ARTICLE

Selective Synthesis of Manganese Oxide Nanostructures for Electrocatalytic Oxygen Reduction

Fangyi Cheng, Jian Shen, Weiqiang Ji, Zhanliang Tao, and Jun Chen*

Institute of New Energy Materials Chemistry and Key Laboratory of Energy Materials Chemistry (Tianjin), Chemistry College, Nankai University, Tianjin 300071, People's Republic of China

ABSTRACT This work presents two points with respect to manganese oxide (MnO_x) nanomaterials: their controllable synthesis with desired phases and shapes together with their applications as catalysts for oxygen reduction and Al/air batteries. Solid MnO_x with crystalline phases of MnOOH, Mn_2O_3, and MnO_2 as well as shapes of the sphere, wire, rod, and particle were prepared through a simple one-pot hydrothermal route. Selective preparation was achieved by adjusting the surfactant concentration that controls simultaneously the growth thermodynamic and dynamic parameters of MnO_x nanocrystals. Electrochemical investigations show that the obtained Mn_2O_3 nanowires, which possess a large aspect ratio and preferentially exposed (222) crystal surfaces, exhibit remarkable catalytic activity (comparable to Pt/C counterparts) toward the electroreduction of oxygen in alkaline media. The tailored MnO_x nanostructures may find prospective applications as low-cost catalysts for alkaline fuel cells and metal/air batteries.

KEYWORDS: manganese oxides • nanostructures • electrocatalytic oxygen reduction • Al/air batteries

INTRODUCTION

Selective synthesis of nanoscale materials with controllable composition and morphology represents an increasingly important research direction in nanosciences and nanotechnologies because the intrinsic properties of nanostructures are generally phase-, shape-, and size-dependent (1, 2). Solution-chemical synthesis has been extensively employed as a versatile "bottom-up" synthetic methodology to synthesize inorganic nanostructures with diverse morphologies (3, 4). In an aqueous system with surfactant, the organic and inorganic interfaces will determine the transporting behaviors of reactive species and thus affect the nucleation and growth of solid nanocrystals (5, 6). However, facile and simultaneous control over the oxidation state, crystal phase, and morphology of nanomaterials remains challenging because of elusive interactive thermodynamic and kinetic parameters.

Fuel cells and metal/air batteries offer attractive alternatives to traditional fossil-fuel systems considering efficient and clean energy production, conversion, and storage (7, 8). Using oxygen in air as the cathode-active materials endows these systems with more profitable energy density and material efficiency. However, one critical issue to be addressed is the lack of effective electrocatalysts for the four-electron (4e) reduction of O_2 (ORR) at relatively low overpotential (9). Although Pt-based metals or alloys have been proven to exhibit the best overall performance for catalyzing ORR (9), their high cost and limited abundance necessitate the exploitation of new nonprecious metal catalysts.

Recently, manganese oxides (MnO_x) have been widely investigated as one of the most promising candidates for ORR in an alkaline medium (10−19); their prominent advantages arise from low cost and toxicity as well as high chemical stability and catalytic activity. In particular, MnO_x-nanostructured materials have received intensive interest for their diverse applications in the fields of catalysis, magnetism, and energy storage and conversion (10−13, 20−22). The properties of MnO_x nanostructures are known to highly depend upon their chemical composition, crystalline phase, and textural morphology (23, 24). Here, we report a one-pot surfactant-assisted approach to the selective preparation of MnO_x materials with simultaneously controlled shape and crystallographic form and, especially, the investigation of their ORR electrocatalytic performance.

EXPERIMENTAL SECTION

Preparation. In a typical synthesis of MnO_2 nanorods/nanowires, 1 mmol of $Mn(NO_3)_2$ (Alfa Aesar) and 0.01 mmol of sodium dodecylbenzenesulfonate (SDBS; analytical grade) were dissolved separately in 10 mL of deionized water and transferred into a 25 mL Teflon-lined autoclave under vigorous magnetic stirring. Then the sealed autoclave containing the homogeneous mixture was maintained at 170 °C for 12 h and allowed to cool naturally to ambient temperature. The resulting solid product was collected by centrifugation, washed with distilled water, and finally dried overnight in air at 60 °C. For the preparation of Mn_2O_3 and MnOOH, similar procedures were carried out except that the ratio of manganese salt to surfactant was altered. Mn_2O_3 nanowires were obtained by starting with 1 mmol of $Mn(NO_3)_2$ and 2 mmol of SDBS, whereas 20 mmol of SDBS was required for the formation of MnOOH microspheres.

Characterization. The phase structures of the as-prepared samples were determined by powder X-ray diffraction (XRD;

* Corresponding author. Fax: (86) 22-2350-6808. E-mail: chenabc@nankai.edu.cn.

Received for review October 18, 2008 and accepted December 12, 2008

DOI: 10.1021/am800131v

Published on Web 01/09/2009

Rigaku D/max-2500 diffractometer with Cu Kα radiation). Morphologies were characterized by scanning electron microscopy (SEM; Philips XL-30 and JEOL JSM-6700F field emission) and transmission electron microscopy (TEM; Philips Tecnai G^2 F20 operating at 200 kV). The oxidation state was analyzed with X-ray photoelectron spectroscopy (XPS; Kratos Axis Ultra DLD spectrometer with an Al Kα X-ray source). Textural properties were measured by N_2 sorption on a BELSORP-mini sorptometer.

Electrochemical Measurements. The working electrode was fabricated by coating catalysts on a glassy carbon substrate. Mn_2O_3 samples were mixed with carbon powders (Carbot, Vulcan-XC72) in the weight ratio of 30:70 to ensure sufficient electronic conductivity. For electrode preparation, a 5 mg sample of this mixture was dispersed in 1 mL of a 2-propanol solution by sonication. Then 5 μL of the resulting homogeneous suspension was carefully dropped with syringe onto a rotation disk electrode (RDE) and a rotation ring-disk electrode (RRDE), which were air-dried to allow solvent evaporation. To determine the weight of the active materials, 5 μL of ink was pipetted onto a quartz container and the dried deposit was weighed with a high-resolution microbalance (Hiden Isochema IGA001). The determined weight was 0.02−0.03 mg, consistent with the desired value (0.025 mg). For comparison, the neat carbon and the benchmark carbon-supported 20 wt % Pt nanoparticles were also fabricated into electrodes through the same procedures.

For voltammetry measurements, a three-electrode cell was used with a KCl-saturated Ag/AgCl reference electrode and a Pt wire as the counter electrode. The electrolyte comprised a 0.1 M aqueous KOH solution. High-purity Ar or O_2 was purged for 20 min before each test. In RRDE tests, the ring potential was kept at 0.3 V vs Ag/AgCl, which is sufficient to enable the complete oxidation of any intermediate peroxide species while not inducing any oxygen evolution reaction. Unless stated, all potentials in the text were referenced to an Ag/AgCl electrode (0.197 V vs reversible hydrogen electrode). The laboratory-made Al/air batteries were assembled with an Al powder anode, a spacer, and an air cathode consisting of a gas diffusion layer and a Mn_2O_3/C catalyst layer (25). Electrochemical tests were carried out at room temperature on a computer-controlled workstation (263A and 2273 potentionstat/galvanostat assembled with model 636, AMETEK PAR).

RESULTS AND DISCUSSION

Controlled Synthesis of Manganese Oxide Nanotructures. The selective synthesis of MnO_x was achieved via decomposition of an acidic $Mn(NO_3)_2$ solution in the presence of SDBS. Aqueous $Mn(NO_3)_2$ in an oxidizing atmosphere may form manganese oxides through the redox reactions of eqs 1−3 (26, 27):

$$2Mn^{2+} + 3H_2O = Mn_2O_3 + 6H^+ + 2e \quad (|E_1^\circ| = 0.49\ V) \tag{1}$$

$$Mn^{2+} + 2H_2O = MnO_2 + 4H^+ + 2e \quad (|E_2^\circ| = 1.23\ V) \tag{2}$$

$$NO_3^- + 2H^+ + e = NO_2 + H_2O \quad (|E_3^\circ| = 0.78\ V) \tag{3}$$

The formation of high-valence Mn species (MnO_2) requires higher energy according to the Gibbs free energy change $\Delta G = -nFE$, where n is the transfer electron numbers, F is the Faraday constant, and E is the reaction potential. The formation of MnO_2 is thermodynamically unforseeable because $E_2° > E_3°$. To obtain MnO_2, a high temperature (>160 °C) under hydrothermal conditions is demanded. On the other hand, E correlates with the chemical activities of the reduced (a_R) and oxidized species (a_O) on the basis of the Nernst equation: $E = E° + (RT/nF)\ln(a_O^u/a_R^v)$, where $E°$ is the standard potential, R is the universal gas constant, T is the absolute temperature, and u and v are stoichiometric numbers. Thus, increasing the concentration of free Mn^{2+} may lower the practical potential and thus decrease the required ΔG, favoring the formation of MnO_2. In contrast, under similar oxidizing conditions, a low Mn^{2+} concentration may result in Mn_2O_3 ($E_1 < E_3$).

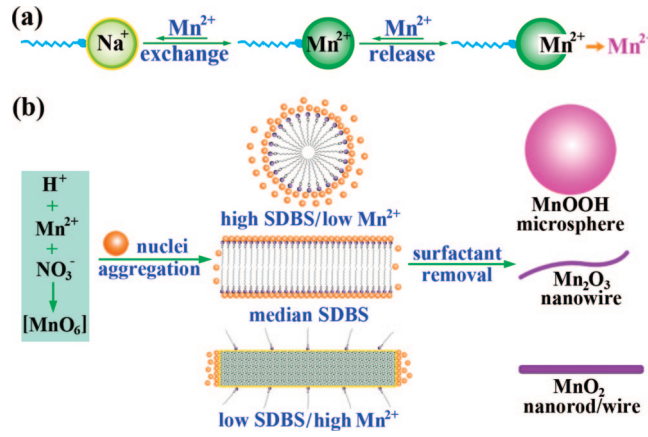

FIGURE 1. Schematic illustration of the controlled synthesis of MnO_x nanostructures: (a) ion exchange between Na^+ and Mn^{2+} to control the amount of reactive free Mn^{2+} in solution; (b) formation of surfactant assemblies and MnO_x solids with different shapes.

Our previous results indicated that the hydrothermal decomposition of $Mn(NO_3)_2$ without surfactant resulted in either pure β-MnO_2 solid or no visible precipitate (24). The morphology of the product depended on the reaction parameters such as the temperature, reactant concentration, and dwell time. In the present study, we employ SDBS as an additional starting material, which plays dual roles of controlling the chemical reaction from both the thermodynamic and kinetic aspects (shown in Figure 1). On the one hand, the amount of SDBS could adjust the free Mn^{2+} concentration in an aqueous solution because of the strong combination effect (Figure 1a and Supporting Information Figure S1). A large quantity of SDBS drastically lowers the concentration of reactive Mn^{2+} and thus facilitates the formation of low-valence manganese oxide. On the other hand, the aggregation between DBS^- and inorganic manganese species could direct the nucleation and crystal growth of MnO_x (Figure 1b). Concentrated surfactant may coassemble with the [MnO_6] octahedral building units to form a spherelike product. In comparison, dilute SDBS acts as a capping and protective agent to promote the anisotropic growth of one-dimensional (1D) nanostructures and to avoid irregular particle aggregation because of the hydrophobic dodecyl chains.

To validate the surfactant-induced selective synthesis, we have performed structural and morphological characterization. Figure 2 shows the XRD data and the related crystallographic structures of the obtained MnO_x. Three patterns can be readily assigned to β-MnO_2 (JCPDS-ICDD card no. 24-735), Mn_2O_3 (card no. 41-1442), and MnOOH (card no. 88-649), respectively. The structural framework of a MnO_x polymorph consists of basic [MnO_6] octahedral units, which

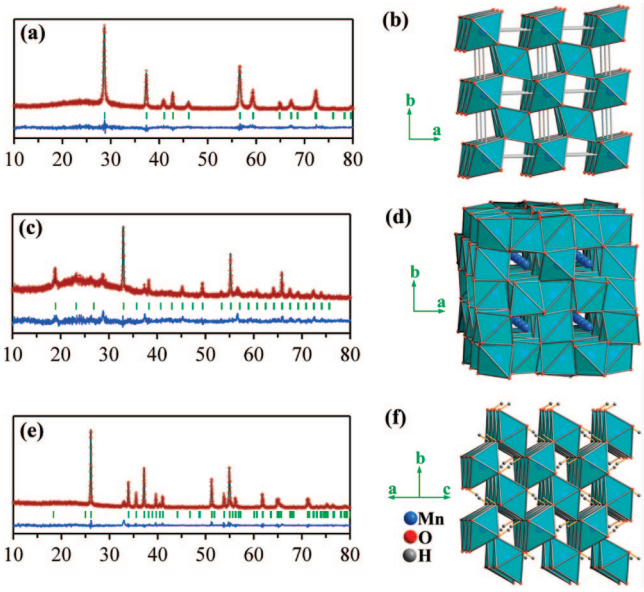

FIGURE 2. (a, c, and e) Rietveld refinement and (b, d, and f) crystal structures of the prepared MnO_x nanostructures. In XRD analysis, the red line is the experimental pattern and the cyan line is the calculated profile; the short green vertical bars below indicate the positions of the allowed Bragg reflections; the bottom blue line shows the difference between the calculated and experimental patterns. (a, b), (c, d), and (e, f) correspond to MnO_2 nanorods/nanowires, Mn_2O_3 nanowires, and MnOOH microspheres, respectively.

are linked in different ways by sharing edges and/or corners (28, 29). The structures of β-MnO_2 and MnOOH appear much alike in the arrangement manner of [MnO_6] units. Both of them possess (1 × 1) tunnels surrounded by four single-octahedron chains and can be viewed as equivalent by replacing O with OH in the crystal lattice. In comparison, the tunnels of Mn_2O_3 are enveloped in eight binding chains, and excess Mn atoms reside in the tunnels because of the higher Mn/O ratio. The dissimilar crystal structure and metal valence of MnO_x will possibly affect their catalytic properties.

The Rietveld refinement of tetragonal MnO_2 gives $a = b = 4.4081(4)$ Å and $c = 2.8784(2)$ Å, with $R_{wp} = 8.93\%$ and $S = 1.5060$ (R_{wp} is the reliability factor, and S is the goodness of fit) (30). The refined result fits well with the experimental data, and the determined cell parameters are in good agreement with the standard values. From the results of the refinement of cubic Mn_2O_3 and monoclinic MnOOH, a very small quantity of MnOOH and MnO_2 is present in the main phase of Mn_2O_3, whereas MnOOH coexists merely with trace Mn_2O_3. A series of MnO_x samples with multiple phases were obtained by adjusting the amount of SDBS from 0.01 to 20 mmol (Supporting Information Figure S2). In addition, we have found that phase control is not attainable when employing an oxidant with strong oxidizing ability. For example, $S_2O_8^{2-}$ yields pure MnO_2 even under extremely low Mn^{2+} and high SDBS concentration, because of the high oxidation potential of persulfate ($S_2O_8^{2-} + 2e = 2SO_4^{2-}$, $E° = 2.01$ V). On the other hand, it is reported that other organic agents such as octadecylamine and ethylenediaminetetraacetate result in low-valence oxides of Mn_3O_4 and MnOOH (31, 32). Therefore, the phase-selective synthesis of MnO_x is achievable by choosing a suitable redox system with organic additives.

The parallel control over the shape and structure of MnO_x is further indicated by the SEM and TEM images shown in Figure 3. Bundles of nanowires were observed for MnO_2 prepared with 0.01 mmol of SDBS, while short rods were obtained without SDBS (Figure 3a,d and Supporting Information Figure S3). In comparison, a very large amount of SDBS results in MnOOH microspheres, which are composed of either aggregating scalelike cones or tightly bound granules (Figure 3c). Interestingly, a median SDBS concentration

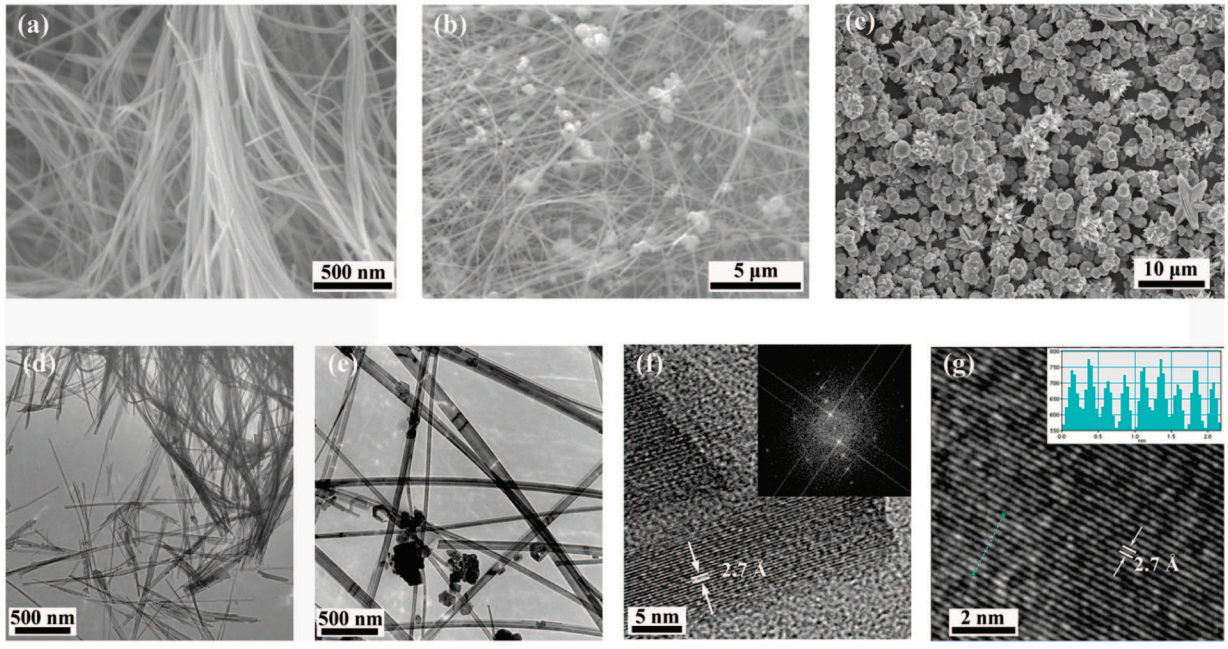

FIGURE 3. SEM micrographs of the selectively synthesized (a) MnO_2, (b) Mn_2O_3, and (c) MnOOH. TEM images of (d) MnO_2 and (e) Mn_2O_3. HRTEM analysis of a single (f) Mn_2O_3 nanowire and (g) nanoparticle. The insets of parts f and g represent the FFT pattern and the line profile, respectively.

yields the Mn_2O_3 product, which is dominated by nanowires with a small proportion (<10%) of nanoparticles (Figure 3b,e). The nanowires show diameters of 10−50 nm and lengths of 20−30 μm, delivering unexpectedly high aspect ratios larger than 1000. Such a high aspect ratio of the 1D nanostructure is uncommon in solution-based synthesis. The morphology control arises from the structure-directing effect of anionic surfactant SDBS, which can self-assemble into spherical or threadlike micelles in an aqueous solution depending on its concentration (Figure 1b). The inorganic species are incorporated into such supramolecular assemblies through electrostatic attraction or complexation (31−33). The nucleation and crystal growth of MnO_x are thereafter confined, leading to the formation of microspheres or nanowires. Furthermore, repulsion and steric hindrance from the surfactant headgroups promote anisotropic growth of elongated 1D nanostructures.

To analyze the structural aspects of the peculiar Mn_2O_3 nanostructures, we have performed high-resolution TEM (HRTEM) imaging on a single wire and particle. Clear lattice fringes can be observed in Figure 3f,g. The neighboring fringes for both the nanowire and nanoparticle are separated by a 2.7 Å distance, corresponding to the spacing between (222) crystal planes of Mn_2O_3. The spotted pattern taken from the reciprocal lattice peak through a two-dimensional Fourier transform (FFT; Figure 3f, inset) indicates that the wire axis elongates along the [111] direction. Careful inspection of nine well-spaced fringes (inset of Figure 3g) also reveals a parallel orientation of (222) planes to the surface of the hexagonal particle. This preferential growth is consistent with XRD analysis (Figure 2c), which shows a very intensive diffraction peak being indexed to the (222) planes. Therefore, the surface of the as-prepared Mn_2O_3 nanostructures is dominated by (222) facets.

The controlled synthesis of MnO_x nanomaterials promotes us to further evaluate the catalytic properties, which is generally considered to be associated with the composition, crystallographic type, and surface state of a catalyst. Before electrochemical investigation, it is necessary to give a brief survey of the ORR mechanism. The oxygen reduction on a classic noble metal catalyst proceeds mainly by a direct 4e pathway (eq 4), which competes with a serial 2 × 2e pathway (34−37). The reaction on MnO_x has been reported to undergo the first partial reduction with two electrons (eq 5) followed by either the 2e reduction (eq 6) or the chemical disproponation (eq 7) of peroxide (10).

$$O_2 + 2H_2O + 4e^- \rightarrow 4OH^- \quad (E^\circ = 0.401\ V) \qquad (4)$$

$$O_2 + H_2O + 2e^- \rightarrow HO_2^- + OH^- \qquad (5)$$

$$HO_2^- + H_2O + 2e^- \rightarrow 3OH^- \qquad (6)$$

$$2HO_2^- \rightarrow 2OH^- + O_2 \qquad (7)$$

Assuming an infinitely rapid and complete HO_2^- reduction/decomposition, the overall reaction of eqs 5−7 is equivalent to that of eq 4, and thus an apparent 4e ORR can be expected. Here we use RDE and RRDE to afford the surfactant-mediated Mn_2O_3 samples and test the ORR catalytic activity in an O_2-saturated alkali electrolyte. Figures 4−6 show the ORR electrochemical performance of Mn_2O_3 nanostructures as well as the comparative carbon (C) and carbon-supported Pt nanoparticles (Pt/C; see the TEM image shown in Supporting Information Figure S4).

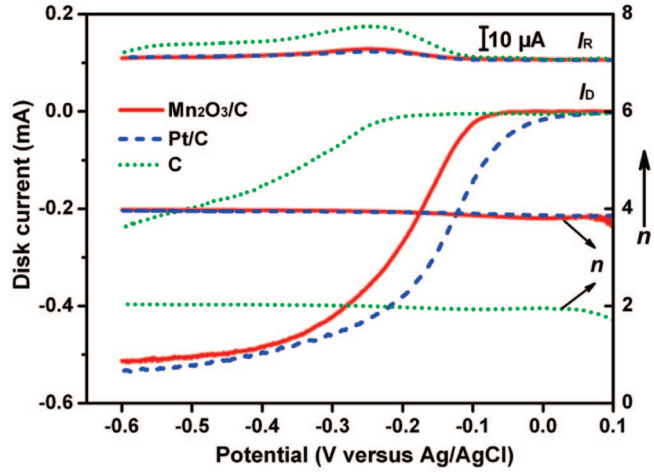

FIGURE 4. RRDE data representing the disk/ring current and the calculated number of electrons (*n*) involved in the ORR for Mn_2O_3/C and the comparative C and Pt/C.

The characteristic catalytic properties from RRDE measurements are summarized in Figure 4. Hydrodynamic voltammetry recorded on the disk for Mn_2O_3/C and Pt/C presents similar shapes with two distinguishable potential regions. Starting at 0.1 V and scanning the potential cathodically, a fast increase of currents in the mixed kinetic-diffusion control region (−0.1 to −0.3 V) is followed by the appearance of diffusion-limiting currents (I_d). Compared with Pt/C, Mn_2O_3/C exhibits a slightly lower onset potential ($E°$) and a very close I_d value. Pure carbon particles, however, show much inferior activity in terms of larger overpotential and smaller current under the same potential. Moreover, the signals detected on the ring electrode are indicative of the amount of intermediate species (i.e., HO_2^-), which are generated from the disk electrode. Thus, Mn_2O_3 nanowires are highly efficient toward peroxide decomposition.

The number of electrons (n) involved in the ORR can be calculated from the ratio of disk and ring currents (I_D and I_R) according to $n = 4 - 2I_R/NI_D$, where N is the collection efficiency of the RRDE (11). The calculated n values at −0.6 V are 2.03, 3.91, and 3.94 for C, Mn_2O_3/C, and Pt/C, respectively. These results suggest an apparent quasi-4e ORR on Mn_2O_3/C with comparable catalytic activities to the benchmark Pt/C catalysts. It should be noted that the ratio of manganese oxides to carbon affects the overall catalytic performance. A series of ratios were tested, and the best Mn_2O_3/C weight ratio was found to be 30:70 considering both the onset potential and the ORR current density (data not shown).

A set of polarization curves (Figure 5a) were recorded on RDE at different rotating speeds to quantitatively verify the apparent 4e reaction on Mn_2O_3/C. High rotational rates accelerate oxygen diffusion to the electrode surface and result in large currents. The current (i) measured at several rotating speeds (ω) under different constant potentials can

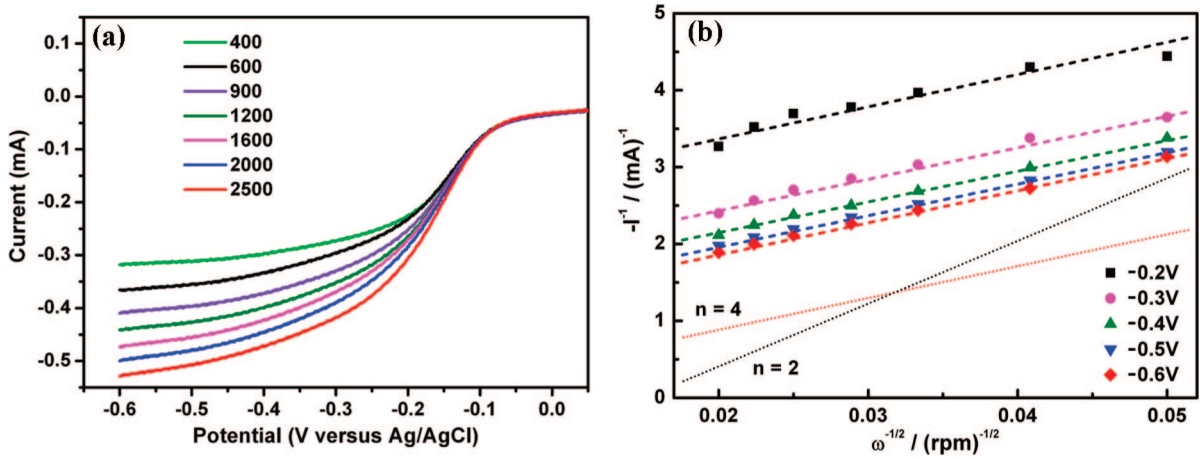

FIGURE 5. (a) Rotation-speed-dependent current−potential curves at a sweeping rate of 1 mV s^{-1}. (b) K−L plots at different potentials for Mn_2O_3/C and the comparative C and Pt/C.

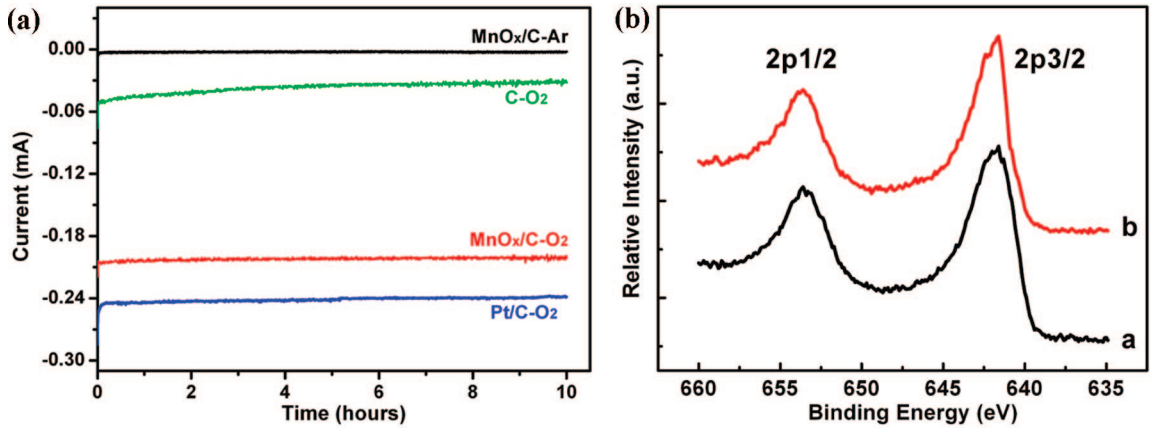

FIGURE 6. (a) Chronoamperometry curves for C, Pt/C, and Mn_2O_3/C catalysts at −0.4 V in a 0.1 M KOH solution saturated with Ar or O_2. (b) Mn 2p XPS spectra of Mn_2O_3 before (curve a) and after (curve b) catalyzing ORR.

be applied to construct Koutecky−Levich (K−L) curves that plot i^{-1} versus $\omega^{-1/2}$ (Figure 5b) based on the K−L equation (38):

$$\frac{1}{i} = \frac{1}{i_k} + \frac{1}{i_d} = \frac{1}{nFAkC^O} - \frac{1}{0.62nFAD_{O_2}^{2/3}\nu^{-1/6}C^O\omega^{1/2}} \quad (8)$$

where i_k is the kinetic current, i_d is the diffusion-limiting current, n is the overall number of transferred electrons, F is the Faraday constant (96500 C mol^{-1}), A is the geometric electrode area (cm^2), k is the rate constant for oxygen reduction, C^O is the saturated O_2 concentration in the electrolyte, D_{O_2} is the diffusion coefficient of O_2, and ν is the kinetic viscosity of the solution. The number of electrons involved in ORR is determined from the slopes of the K−L curves. The standard lines corresponding to $n = 2$ and 4 are also supplemented as a reference. At steady potentials of −0.6 to −0.2 V, the calculated n value is approaching 4. In the absence of Mn_2O_3, the neat Vulcan carbon particles display a poor performance with a n value close to 2 (see Supporting Information Figure S5).

Chronoamperometry curves (Figure 6a) provide further information about the electrochemical activity and stability of the catalysts for oxygen reduction. The catalytic stability of Mn_2O_3 nanowires is clearly illustrated by the steady ORR currents in the polarization period of 10 h. Previously reported carbon-supported MnO_x nanoparticles have also shown almost negligible fade in ORR activity while maintaining similar crystalline and chemical structures under mild aging conditions although a dramatic change occurs by premature aging (39). The determined average current densities are 0.25, 1.66, and 1.92 mA cm^{-2} for C, Mn_2O_3/C, and Pt/C, respectively, at −0.4 V vs Ag/AgCl. The corresponding mass activities are 26.6 and 48.1 mA mg^{-1} with respect to the amount of Mn_2O_3 and Pt, respectively. These data are similar to previous results (10) and ascertain the remarkable catalytic properties of the as-prepared Mn_2O_3. Considering the compromise between performance and price, the low-cost and abundant manganese oxides are therefore promising alternatives to noble metal catalysts for ORR in alkaline media. Figure 6b displays the XPS profiles of Mn_2O_3 samples before and after ORR, showing similar shapes and peak positions. The binding energy of Mn 2p peaks can be assigned to Mn_2O_3 (40) and thus preliminarily confirm the chemical stability under our testing conditions. More physicochemical characterizations at severe operation conditions are ongoing to obtain further stability information.

The above-illustrated favorable catalytic performances of Mn_2O_3 nanostructures prompt us to further employ them for metal/air batteries. As a simple demonstration, Al/air batteries of coin type were assembled with an Al powder anode (20 mg) and an air electrode comprising the catalyst layer

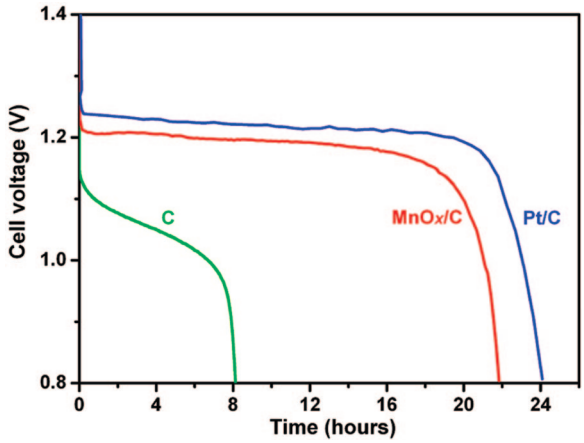

FIGURE 7. Typical galvanostatic discharge profiles of the Al/air batteries assembled with three types of air electrodes.

of MnO_x/C and the comparative C and Pt/C. Figure 7 displays the typical discharge profiles of the laboratory-made Al/air cells at a constant current of 0.4 mA. During cell discharge, aluminum at the anode is consumed and converted to aluminum oxides while oxygen from the air is electrochemically reduced at the cathode. The cells based on MnO_x/C and Pt/C exhibit flat discharge curves with open-circuit voltages (V_{oc}) of 1.56 and 1.61 V and working voltage plateaus of 1.21 and 1.23 V, respectively. It is noted that the MnO_x/C cell delivers a considerably high capacity of 8.74 mAh, which is comparable to that of the Pt/C cell. The cell with neat carbon is not capable of sustaining the current drain, showing lower V_{oc} (1.35 V), continuously fading working voltages, and unfavorable capacity. The variation in the cell performance is doubtlessly derived from the air electrode because the same anode is used in all cells. The Mn_2O_3 nanostructures possess high ORR activities in aspects of moderate onset potential and large current density (Figures 4–6), which enable instantaneous consumption of electrons transferred from the Al anode and thus result in an outstanding performance in the Al/air batteries.

It has been reported that MnO_x is highly catalytically active toward the peroxide decomposition reaction (10–16). In this context, in addition to the direct 4e pathway (eq 4), ORR can proceed through a first step of reducing O_2 to the intermediate HO_2^-, followed by a nearly simultaneous further reduction of HO_2^- to OH^- (eqs 5–7). The latter so-called 2 × 2e ORR pathway is boosted synergistically with the redox shift among manganese species of Mn^{II}, Mn^{III}, and Mn^{IV}. This effect accounts intrinsically for the overall high ORR catalytic activities of MnO_x, as extensively studied by several research groups (10–19). Additional beneficial factors arise from the textural and structural characteristics of Mn_2O_3 nanostructures. The high aspect ratio and the preferential growth direction of thin Mn_2O_3 nanowires provide more (222) surfaces and manganese active sites exposed to the solution (Figure 8). Moreover, the mixture of Mn_2O_3 and carbon possesses a high specific surface area (153 $m^2\ g^{-1}$, shown in Supporting Information Figure S6). All of these features might facilitate the adsorption of O_2, the electron transportation, and the contact between the electrolyte and catalyst, thus resulting in the prominent catalytic performance.

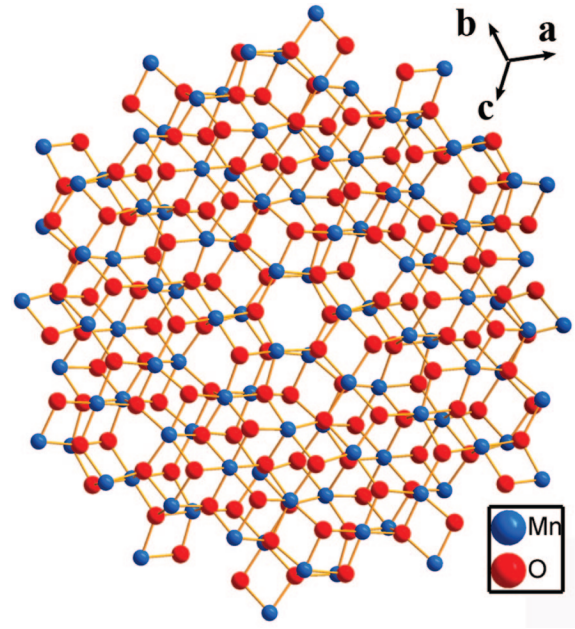

FIGURE 8. Surface cleavage of the preferentially formed (222) face of the Mn_2O_3 crystal showing numerous manganese active sites.

CONCLUSIONS

In conclusion, manganese oxide nanostructures have been selectively synthesized with diverse crystal phases and morphologies through a facile surfactant-assisted hydrothermal route. The obtained Mn_2O_3 nanowires can be applied as catalysts for electrochemical oxygen reduction with quasi-4e transfer. They exhibit considerably high catalytic activities comparable with the benchmark carbon-supported Pt nanoparticles. The present results indicate the potential applications of manganese oxide nanostructures as alternative low-cost catalysts for alkaline fuel cells and metal/air batteries.

Acknowledgment. This work was supported by the National 973 (Grant 2005CB623607) and 863 (Grant 2007AA05Z124) and Tianjin High-Tech (Grant 07ZCGHHZ00700).

Supporting Information Available: Experimental details, additional characterization (XRD patterns and SEM/TEM images) of the Mn–SDBS precursors and MnO_x samples, N_2 sorption isotherms, and ORR catalytic properties of the neat carbon powders. This material is available free of charge via the Internet at http://pubs.acs.org.

REFERENCES AND NOTES

(1) Hu, J.; Odom, T. W.; Lieber, C. M. *Acc. Chem. Res.* **1999**, *32*, 435–445.
(2) Burda, C.; Chen, X.; Narayanan, R.; El-Sayed, M. A. *Chem. Rev.* **2005**, *105*, 1025–1102.
(3) Cushing, B. L.; Kolesnichenko, V. L.; O'Connor, C. J. *Chem. Rev.* **2004**, *104*, 3893–3946.
(4) Xia, Y. N.; Yang, P. D.; Sun, Y. G.; Wu, Y. Y.; Mayer, B.; Gates, B.; Yin, Y. D.; Kim, F.; Yan, H. Q. *Adv. Mater.* **2003**, *15*, 353–389.
(5) Wang, X.; Peng, Q.; Li, Y. D. *Acc. Chem. Res.* **2007**, *40*, 635–643.
(6) Rao, C. N. R.; Kalyanikutty, K. P. *Acc. Chem. Res.* **2008**, *41*, 489–499.
(7) Steele, B. C. H.; Heinzel, A. *Nature* **2001**, *414*, 345–352.

(8) Winter, M.; Brodd, J. B. *Chem. Rev.* **2004**, *104*, 4245–4269.
(9) Kinoshita, K. *Electrochemical Oxygen Technology*; Wiley: New York, 1992.
(10) Chaînet, I. R.; Chatenet, M.; Vondrák, J. *J. Phys. Chem. C* **2007**, *111*, 1434–1443.
(11) El-Deab, M. S.; Ohsaka, T. *Angew. Chem., Int. Ed.* **2006**, *45*, 5963–5966.
(12) Gong, K.; Yu, P.; Su, L.; Xiong, S.; Mao, L. *J. Phys. Chem. C* **2007**, *111*, 1882–1887.
(13) Xu, J. J.; Yang, J. *Electrochem. Commun.* **2003**, *5*, 306–311.
(14) Ohsaka, T.; Mao, L.; Arihara, K.; Sotomura, T. *Electrochem. Commun.* **2004**, *6*, 273–277.
(15) Mao, L.; Zhang, D.; Sotomura, T.; Nakatsu, K.; Koshiba, N.; Ohsaka, T. *Electrochim. Acta* **2003**, *48*, 1015–1021.
(16) Mao, L.; Sotomura, T.; Nakatsu, K.; Koshiba, N.; Zhang, D.; Ohsaka, T. *J. Electrochem. Soc.* **2002**, *149*, A504–A507.
(17) Lima, F. H. B.; Calegaro, M. L.; Ticianelli, E. A. *J. Electroanal. Chem.* **2006**, *590*, 152–160.
(18) Verma, A.; Jha, A. K.; Basu, S. *J. Power Sources* **2005**, *141*, 30–34.
(19) Cao, Y. L.; Yang, H. X.; Ai, X. P.; Xiao, L. F. *J. Electroanal. Chem.* **2003**, *557*, 127–134.
(20) Espinal, L.; Suib, S. L.; Rusling, J. F. *J. Am. Chem. Soc.* **2004**, *126*, 7676–7682.
(21) Seo, W. S.; Jo, H. H.; Lee, K.; Kim, B.; Oh, S. J.; Park, J. T. *Angew. Chem., Int. Ed.* **2004**, *43*, 1115–1117.
(22) Cheng, F. Y.; Chen, J.; Gou, X. L.; Shen, P. W. *Adv. Mater.* **2005**, *17*, 2753–2756.
(23) Devaraj, S.; Munichandraiah, N. *J Phys. Chem. C* **2008**, *112*, 4406–4417.
(24) Cheng, F. Y.; Zhao, J. Z.; Song, W. E.; Li, C. S.; Ma, H.; Chen, J.; Shen, P. W. *Inorg. Chem.* **2006**, *45*, 2038–2044.
(25) Li, C. S.; Ji, W. Q.; Chen, J.; Tao, Z. L. *Chem. Mater.* **2007**, *19*, 5812–5814.
(26) Bard, A. J.; Parsons, R.; Jordan, J. *Standard Potentials in Aqueous Solution*; Marcel Dekker: New York, 1985.
(27) http://web.archive.org/web/20070518092613/www.northland.cc.mn.us/Chemistry/standard_reduction_potentials.
(28) Wang, X.; Li, Y. D. *J. Am. Chem. Soc.* **2002**, *124*, 2880–2881.
(29) Xiong, Y.; Xie, Y.; Li, Z.; Wu, C. *Chem.—Eur. J.* **2003**, *9*, 1645–1651.
(30) Izumi, F.; Ikeda, T. *Mater. Sci. Forum* **2000**, *321—324*, 198–203.
(31) Oaki, Y.; Imai, H. *Angew. Chem., Int. Ed.* **2007**, *46*, 4951–4955.
(32) Wang, D. S.; Xie, T.; Peng, Q.; Zhang, S. Y.; Chen, J.; Li, Y. D. *Chem.—Eur. J.* **2008**, *14*, 2507–2513.
(33) Huo, Q.; Margolese, D. I.; Ciesla, U.; Demuth, D. G.; Feng, P.; Gier, T. E.; Sieger, P.; Firouzi, A.; Chmelka, B. F.; Schüth, F.; Stucky, G. D. *Chem. Mater.* **1994**, *6*, 1176–1193.
(34) Antoine, O.; Durand, R. *J. Appl. Electrochem.* **2000**, *30*, 839–844.
(35) Chatenet, M.; Aurousseau, M.; Durand, R.; Andolfatto, F. *J. Electrochem. Soc.* **2003**, *150*, D47–D55.
(36) Chatenet, M.; Genies-Bultel, L.; Aurousseau, M.; Durand, R.; Andolfatto, F. *J. Appl. Electrochem.* **2002**, *32*, 1131–1140.
(37) Schneider, A.; Colmenares, L.; Seidel, Y. E.; Jusys, Z.; Wickman, B.; Kasemo, B.; Behm, R. J. *Phys. Chem. Chem. Phys.* **2008**, *10*, 1931–1943.
(38) Wang, C.; Daimon, H.; Onodera, T.; Koda, T.; Sun, S. *Angew. Chem., Int. Ed.* **2008**, *47*, 3588–3591.
(39) Roche, I.; Chaînet, E.; Chatenet, M.; Vondrák, J. *J. Appl. Electrochem.* **2008**, *38*, 1195–1201.
(40) Tan, B. J.; Klabunde, K. L.; Sherwood, P. M. A. *J. Am. Chem. Soc.* **1991**, *113*, 855–861.

AM800131V